

# HSIDMamba: Exploring Bidirectional State-Space Models for Hyperspectral Denoising

Yang Liu, Jiahua Xiao, Yu Guo<sup>✉</sup>, Peilin Jiang, Haiwei Yang, Fei Wang

**Abstract**—Effectively discerning spatial-spectral dependencies in HSI denoising is crucial, but prevailing methods using convolution or transformers still face computational efficiency limitations. Recently, the emerging Selective State Space Model(Mamba) has risen with its nearly linear computational complexity in processing natural language sequences, which inspired us to explore its potential in handling long spectral sequences. In this paper, we propose HSIDMamba(HSDM), tailored to exploit the linear complexity for effectively capturing spatial-spectral dependencies in HSI denoising. In particular, HSDM comprises multiple Hyperspectral Continuous Scan Blocks, incorporating BCSM(Bidirectional Continuous Scanning Mechanism), scale residual, and spectral attention mechanisms to enhance the capture of long-range and local spatial-spectral information. BCSM strengthens spatial-spectral interactions by linking forward and backward scans and enhancing information from eight directions through SSM, significantly enhancing the perceptual capability of HSDM and improving denoising performance more effectively. Extensive evaluations against HSI denoising benchmarks validate the superior performance of HSDM, achieving state-of-the-art results in performance and surpassing the efficiency of the latest transformer architectures by 30%.

**Index Terms**—Hyperspectral image denoising; selective state space models; bidirectional continuous scan;

## I. INTRODUCTION

**H**YPERSPECTRAL images(HSI) refers to a type of remote sensing data that captures surface features across a broader spectrum of wavelengths. HSI includes the spectral characteristics of objects reflecting or emitting light of different wavelengths, and its unique spectral characteristics enable it to store more comprehensive information. Therefore, HSI has applications in various fields, including remote sensing, object detection, classification, image processing, and more [1]–[5].

The presence of noise in HSI is a multi-faceted issue, stemming from an array of sources including sensor imperfections, atmospheric disturbances, extraneous light reflections from surfaces, and malfunctioning of the capturing equipment. These pervasive noise contributors significantly degrade the quality and precision of hyperspectral data, thereby undermining its dependability for real-world applications. As a

The authors are with the National Key Laboratory of Human-Machine Hybrid Augmented Intelligence, National Engineering Research Center for Visual Information and Applications, and Institute of Artificial Intelligence and Robotics, Xi'an Jiaotong University, Xi'an, Shaanxi 710049, China, and with the school of software, Xi'an Jiaotong University, Xi'an, Shaanxi 710049, China(e-mail: (1228754216, xjh847286495)@stu.xjtu.edu.cn, (yu.guo, pljiang, wfx)@xjtu.edu.cn, yanghw09@163.com

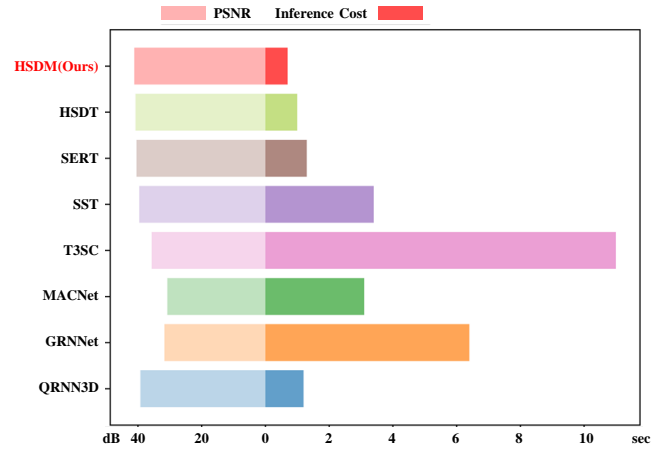


Fig. 1. Quantitative comparisons (PSNR (dB) vs. Inference Cost(second)) of our HSDM against other deep learning methods on ICVL datasets under mixture noise.

result of such noise contamination, the integrity of data-driven outcomes, including classification, localization, and analytical tasks, is compromised. This can have detrimental consequences on the veracity and efficacy of decision-making processes that rely on HSI. In recognition of these challenges, the imperative to efficiently suppress noise from HSI is underscored.

In contrast to traditional RGB and grayscale images, HSI contains a wealth of spectral information, posing two significant challenges: substantial redundancy in the spectral domain and computational burden associated with capturing long-range contextual dependencies. Prior assumptions about hyperspectral noise constrain traditional model-based approaches and require adjustments of different hyperparameters for varying scenes [6]–[8]. These limitations constrain their performance on real-world datasets and necessitate significant computational and temporal resources. Conversely, recent efforts leveraging deep learning networks have demonstrated superiority in hyperspectral denoising tasks, notably through architectures designed around convolutional neural networks(CNN) and transformer frameworks.

While the prospects for hyperspectral image restoration based on CNNs are promising, existing work in this domain also encounters several challenges. Firstly, the weight-sharing strategy inherent in CNNs constrains the model's ability to dynamically adapt to different inputs, potentially affecting its performance when dealing with unseen low-quality images.

Secondly, the limited receptive field of individual convolutional layers, constrained by the size of the kernel, may significantly increase local restoration biases. Although some studies have proposed different convolution designs, current CNN-based restoration methods are still constrained by the effective receptive field [9], [10].

Subsequent Transformer architectures effectively addressed the limitations of receptive fields, leading to significant advancements in long-range dependency modeling and model performance. However, the inherent computational and memory complexity of the self-attention mechanism employed by Transformers results in quadratic growth in computational burden and memory requirements as sequence length increases [11]–[13].

State Space Models (SSMs) have attracted significant research interest in addressing the challenge of modeling long sequences. They can be viewed as a fusion of recurrent neural networks (RNNs) and CNNs. Notable contributions in this domain include the Structured State Space (S4) [14] and its various extensions [15]–[17]. The recent development, Mamba [18], further enhances the S4 framework by incorporating a selection mechanism, enabling the model to focus on relevant information in an input-dependent manner. Additionally, hardware-aware optimizations are applied to ensure efficient training and inference. Mamba surpasses Transformers in handling large-scale datasets and exhibits linear scalability with sequence length, positioning it as a promising alternative for language modeling tasks. Concurrent research efforts have extended this architecture beyond 1D language tasks to 2D visual domains [19]–[21], including tasks such as image classification and biomedical image segmentation. However, to our knowledge, there has been no exploration of leveraging this efficient architecture for addressing HSI denoising.

Given the inherent long sequences generated by HSI, which necessitate the capabilities of Mamba, we propose Hyperspectral Denoising Mamba(HSDM), an effective model based on the selective state space model. HSDM harmoniously eliminated the shortcomings of convolution and attention mechanisms, enabling better modeling of spatial-spectral long-range dependencies in linear complexity. Moreover, HSDM introduces a multi-bidirectional continuous scanning mechanism(BCSM) tailored for HSI. Specifically, BCSM efficiently integrates information from multiple directions processed by designing forward and backward contiguous flattening SSM mechanisms, enhancing the performance of HSDM through residual and spectral attention mechanisms. As illustrated in Figure 1, HSDM achieves state-of-the-art performance in denoising and inference speed, demonstrating a well-balanced approach.

Experimental outcomes across diverse datasets validate the superior performance of our proposed HSDM compared to existing methodologies, evidenced by both objective metrics on synthetic datasets and visual quality assessments on real datasets. To summarize, the key contributions of our study are outlined below:

- We are the first to introduce a simple and effective Bidirectional State-Space Model, thereby devising a novel

architecture distinct from CNNs and transformers for HSI denoising.

- Addressing the inherent spatial and spectral correlations in HSI data, we propose a novel Continuous Bidirectional Scanning Mechanism to explore tailored variations of the Mamba framework.
- Extensive experiments demonstrate that our proposed MambaHSID achieves state-of-the-art performance and is 30% faster than the latest transformer method, offering a more balanced solution in terms of performance and efficiency for HSI denoising.

## II. RELATED WORK

### A. Convolutional Neural Networks

CNNs have attracted significant attention for their ability to automatically extract noise patterns without prior knowledge of noise types. [22] leverage 2D convolutions effectively for HSI denoising, showing strong performance in both spatial and spectral domains. Additionally, some approaches utilizing 3D convolutions, exemplified by the works [9], [23], excel in capturing spatial-spectral structural information in high-dimensional data. Among these methods, QRNN3D [10], stands out for effectively modeling spatial-spectral dependencies and global spectral correlations, fully exploiting the interplay between spatial and spectral dimensions. Additionally, [24] employs a non-local neural network with end-to-end model assistance, incorporating considerations of both spectral low-rankness and spatial depth priors to mitigate HSI noise. Nonetheless, despite their impressive noise reduction capabilities, CNNs inherently local receptive fields may restrict their ability to capture long-range dependencies within the data.

### B. Vision Transformer

The Vision Transformer (ViT) has gained traction in computer vision, employing a unique architecture from traditional CNNs by leveraging the Transformer model initially designed for natural language processing. ViT excels across various tasks such as image classification, object detection, and segmentation due to its ability to handle images of any size and exhibit strong generalization capabilities.

ViT divides input images into patches and transforms the pixel data of each patch into a one-dimensional sequence, which is processed through multiple Transformer layers. The self-attention mechanism enables complex dependencies between pixels, capturing global information within the image.

In recent research on hyperspectral imaging with the Transformer architecture, innovative approaches have been proposed. For instance, [25] introduces a grouped pixel embedding module for HSI classification within local spatial-spectral contexts. [26] customize a mask-guided mechanism for effective HSI super-resolution, while [27] enhance denoising capabilities using window attention modules and global spectral attention to focus on spatial similarity and spectral dependencies.

However, despite its aptitude for capturing global interactions, Transformer suffers computational and data efficiency

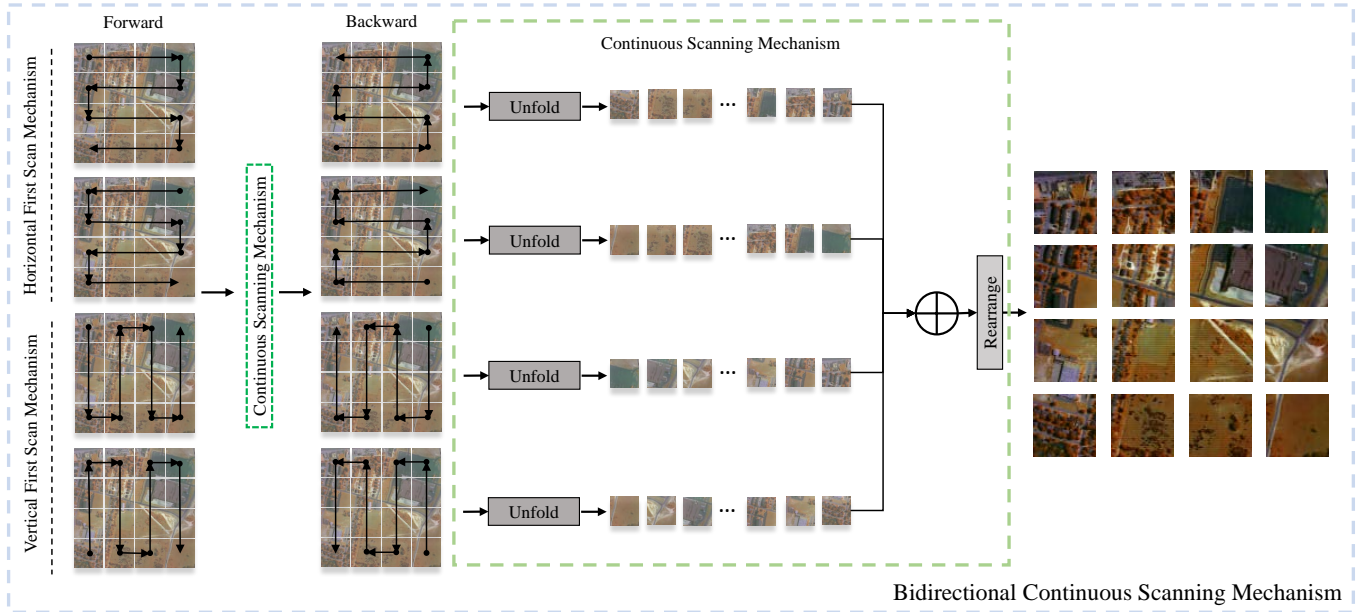


Fig. 2. Overall of the continuous spatiotemporal scanning mechanism. Sequentially passing through forward and backward continuous scanning mechanisms not only saves space and training time for the model but also better explores the spatial-spectral continuity of HSI.

hampered by its requirement for large-scale datasets for training and its tendency to be computationally intensive, especially when dealing with high-resolution HSI.

### C. State Space Models

Recent developments in state space models (SSMs) have shown a marked proficiency in encapsulating the dynamic interconnections and dependencies prevalent in language sequences. The S4 model, which specifically engineered to adeptly navigate long-range dependencies without sacrificing linear computational complexity, represents a significant stride in this research area. Expanding on these gains, the Mamba framework [18] introduces an SSM layer that adapts to data and a parallel scanning selection mechanism, which collectively exhibits enhanced capability in processing extensive sequences with linear complexity—a considerable advantage over attention-based transformers as noted in [12], [13].

In the domain of visual processing, SSMs have equally made impactful inroads. Applications of SSMs have been applied to visual tasks such as image classification [28] as well as in discerning long-range temporal dependencies within movie clip classification scenarios [29]. The advent of methodologies has heralded a period of innovation for state space models. Notably, the Mamba model distinguishes itself with its cutting-edge selective SSM feature, attaining an equipoise of linear computational complexity with the capacity to model long-term dynamics effectively. Our proposed HSDM innovation enhances the original Mamba model by optimizing its data-dependent state space layer for advanced HSI denoising efficiency and effectiveness.

## III. METHODS

In this section, we first introduce the basic concepts of state space models, the implementation details of mamba, and the

details of our proposed HSDM architecture.

### A. Preliminaries

**State space models** is a statistical model used to describe the evolution of a system over time. SSM typically models input data and hidden states for input sequences using Ordinary Differential Equations (ODE). A linear SSM can be represented as:

$$\begin{aligned} h'(t) &= \mathbf{A}h(t) + \mathbf{B}x(t) \\ y(t) &= \mathbf{C}h(t) + \mathbf{D}x(t) \end{aligned} \quad (1)$$

where  $x(t) \in \mathbb{R}^L$  represents the input sequence,  $h(t) \in \mathbb{R}^N$  is hidden state, which assist in mapping  $x(t)$  to  $y(t) \in \mathbb{R}^M$ . Among the formula,  $\mathbf{A} \in \mathbb{R}^{N \times N}$ ,  $\mathbf{B} \in \mathbb{R}^{N \times 1}$ ,  $\mathbf{C} \in \mathbb{R}^{1 \times N}$ ,  $\mathbf{D} \in \mathbb{R}$ .  $N$  represents the hidden state size.

Subsequently, Eq.1 are usually merged using a discretization process, which can be represented as follows:

$$\begin{aligned} \bar{\mathbf{A}} &= \exp(\Delta \mathbf{A}) \\ \bar{\mathbf{B}} &= (\Delta \mathbf{A})^{-1} (\exp(\Delta \mathbf{A}) - I) \cdot \Delta \mathbf{B} \end{aligned} \quad (2)$$

where  $\Delta$  represents the time scale parameter, used to convert continuous parameters  $\mathbf{A}$  and  $\mathbf{B}$  into discrete parameters  $\bar{\mathbf{A}}$  and  $\bar{\mathbf{B}}$ . The zero-order hold (ZOH) method is commonly used for this discretization.

After discretization, the discrete version Eq.1 can be rewritten as:

$$\begin{aligned} h_t &= \bar{\mathbf{A}}h_{k-1} + \bar{\mathbf{B}}x_k \\ y_t &= \mathbf{C}h_k + \mathbf{D}x_k \end{aligned} \quad (3)$$

In neural sequence modeling architectures, this discretized stack allows for learning the parameters of each layer through gradient descent. Recently, Selective State Space Models (termed Mamba) [29] have significantly enhanced the flexibility of SSMs by relaxing the time-invariance constraints on

SSM parameters while preserving computational efficiency. Multiple works have demonstrated Mamba’s advantage in modeling long-range dependencies.

**Bidirectional Selective SSM.** By employing highly efficient parallel scanning, Mamba mitigates the impact of repetitive sequential nature. However, for hyperspectral data, the original Mamba one-way perception mechanism is not sufficient for analyzing hyperspectral data. Considering the continuity of spatial features, MambaHSID designed a bidirectional continuous Mamba scanning block to better model the sequence bi-directional by designing 8 different scanning starting points and directions. In this study, we explored Mamba’s continuous scanning mechanism for hyperspectral data by continuously processing 1D sequences using forward-backward SSM, to maximize the inductive bias of similarity in multidimensional data.

### B. HSID Mamba Model

1) *Overall Architecture:* As illustrated in Figure 3, our proposed architecture of HSIDMamba(HSDM) comprises a shallow feature extractor followed by multiple layers of Hyperspectral Continuous Scan Layers (HCSL). The HCSL integrates a 2D spatial continuous scanning mechanism with a channel attention component. Initially, the HSI input undergoes feature extraction via the shallow feature extractor. Subsequently, these shallow features are fed into the HCSL. Through scaling and skip connections, the input undergoes 1D convolution before being passed into the Mamba-scan module, where the resulting anisotropic vectors are combined.

$$\begin{aligned} F_s &= K_1 \otimes Y_i n \\ F' &= HCSL(F_s) \\ Y_{out} &= Denoiser(F') \end{aligned} \quad (4)$$

where  $Y_i n$  represents the input noise HSI,  $K_1$  is a  $3 \times 3$  convolutional kernel,  $\otimes$  denotes the convolutional operation, and  $F_s, F'$  represents the shallow feature, intermediate feature. After multi-layer extraction, a Denoiser is used to suppress HSI noise, represented as  $Y_{out}$ .

---

#### Algorithm 1 Learning strategy for HSDM.

---

**Input:**  $\{x_1, \dots, x_n\} \in \mathbb{R}^{H \times W \times B}$   
**Output:**  $\theta$   
**Hyperparameters:**  $Epoch_t, t \in \{0, \infty\}$   
**For**  $i = 1, 2, \dots, Epoch_t$   
     $B, C, H, W \leftarrow Shape(x_i)$   
     $F \leftarrow LayerNorm(Reshape(x, (B, C, L)))$   
     $F_{forward} \leftarrow SSM(rearrange(linear(F)))$   
     $F_{Backward} \leftarrow SSM(rearrange_b(linear(F)))$   
     $F_{proj} \leftarrow SiLU(F)$   
     $F_{out} \leftarrow F_{proj} \times F_{forward} + F_{proj} \times F_{Backward}$   
     $y_{HMSB} \leftarrow CA(Conv(LN(F + F_{out})))$   
     $y_i \leftarrow x_i + Conv(y_{HMSB})$   
     $P(\theta) \leftarrow (y_i, x_i | \theta)$   
     $loss(\theta) \leftarrow -\sum_{j=1}^n \log P(\theta)[x_n[j+1], x_n[j]]$   
     $\theta \leftarrow \theta - \nabla loss(\theta)$   
**return**  $\theta$

---

2) *Hyperspectral Continuous Scan Block:* Upon entering the HCSL, the shallow features remain in their 2D representation. The overall network algorithm flowchart is shown in Algorithm1(a). To further process the data, we apply layer normalization for rearrangement, unfolding it into 1D data. Subsequently, this 1D data is passed through a 1D convolutional layer before entering the BSSM (Bidirectional State Space Model) layer.

$$\begin{aligned} F_{tmp} &= BSSM(LN(F_{in})) + F_{in} \\ F_{out} &= CA(Conv(LN(F_{tmp}))) + F_{tmp} \end{aligned} \quad (5)$$

As depicted in Figure 2, to conduct a comprehensive analysis of state selection outcomes, we aggregated the results obtained from various scans, employing two rounds of normalization. For an intermediate feature derived from the Hyperspectral Continuous Scan Block(HCSB), denoted as  $F'_i$ , the subsequent output feature  $F'_{i+1}$  of the HCSB can be precisely articulated as follows:

$$\begin{aligned} F_j &= Fold(rearrange(F'_i)), j = 0, 1, \dots, t \\ F_{i+1} &= UnFold(LN(\sum_{j=0}^t LN(SS2D(F_j)))) \end{aligned} \quad (6)$$

where  $F_j$  represents the reordered 2D features, and  $t$  represents the number of rearranged sequences.

### C. Complexity Analysis

In previous work, CNNs and Transformers were two common architectures that played important roles in processing sequence and image data. Compared to traditional CNNs and Transformers, HSDM takes advantage of linear complexity. The time complexity of traditional CNNs depends on the size of the input image and the number of filters, while the time complexity of Transformers is quadratic with the length of the input sequence. Here we analyze their time complexity.

**Convolutional neural networks:** The computational complexity of the conventional Convolutional Neural Networks (CNNs) architecture can be succinctly expressed as follows:

$$\Omega(T) = \Omega(K^2 \times H \times W \times C) \quad (7)$$

where  $k$  is convolutional kernel size,  $H, W, C$  denotes the input feature dimension.

**Transformer with Self-Attention:** The computational complexity of the conventional global self-attention transformer architecture can be mathematically represented as follows:

$$\Omega(T) = \Omega(H \times W \times C^2) \quad (8)$$

**Transformer with Cross-Attention:** The formula describing the computational complexity of the Cross-Attention transformer architecture can be succinctly expressed as follows:

$$\Omega(CSSA) = \left( \frac{H^2 W^2 \times C^2}{h \times w} \right) \quad (9)$$

where  $W$  denotes the input feature windows with sizes  $[h, w]$ .

**HSID Mamba:** The formula for HSDM architecture can be expressed as:

$$\Omega(HSIDM) = (T \times H \times W \times C) \quad (10)$$

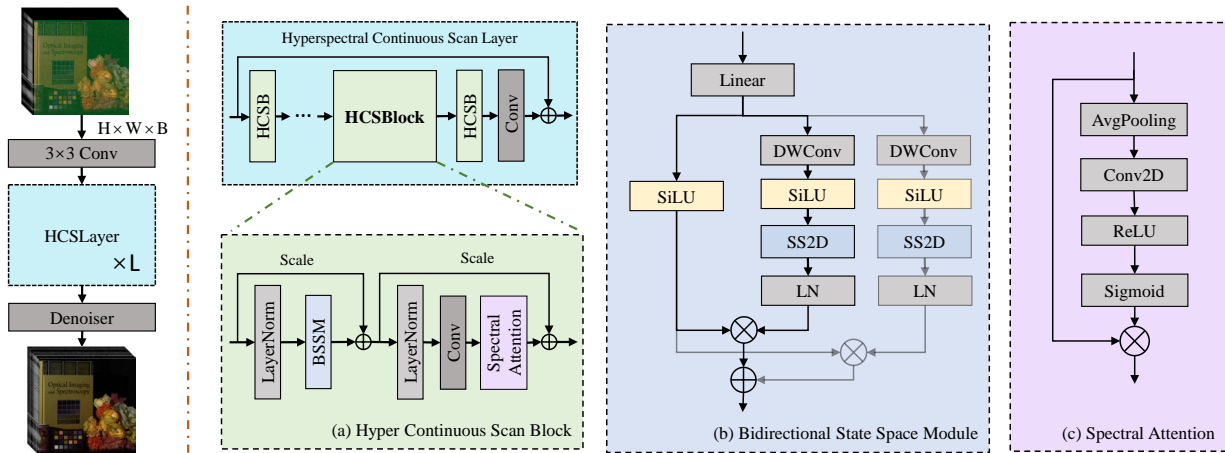


Fig. 3. Overall framework of our proposed Hyperspectral Denoising Mamba. Adopting the holistic architecture of ViT, we integrate bidirectional continuous scanning mechanism, BSSM (b), and spectral attention (c) through the core component, HCSB (a).”

where  $T$  represents the number of times to rearrange 2D features.

Therefore, when dealing with lengthy sequence data, HSDM offers distinct advantages over conventional CNNs and Transformers. HSDM excels in handling extended sequence data with greater efficiency, all while minimizing the computational overhead typically associated with HSI Denoising.

#### IV. EXPERIMENTS

In this section, we explore both synthetic, real, and remote datasets being corrupted by mixed noise. We extensively assess our proposed HSDM and conduct experiments to analyze its efficacy thoroughly.

##### A. Overall Network Architecture

As illustrated in Figure 3, in the baseline configuration of HSDT, we employed a total of 3 layers of HCSL, each comprising 4 Blocks for alternating forward and backward Continuous Scan. Additionally, prior to the modules, a residual connection and feature concatenation from the module output were utilized. Finally, skip connections were employed to add the initial input of each layer to the overall layer output, ensuring the stability of the denoising pattern.

1) *Training Datasets*: In training our proposed HSDM, we adopt a dataset configuration similar to that of [30], where 100 images are randomly sampled from the ICVL dataset [31]. These images are centrally cropped to achieve a spatial resolution of 512×512 with 31 spectral bands. Further adjustments are made to the spatial resolution of the images to 64×64 through operations including random cropping, rotation, and flipping, resulting in approximately 53,000 training samples.

2) *Testing Datasets*: Our experimental setup encompasses datasets including ICVL and CAVE [32], representing synthetic scenarios. Specifically, for the ICVL test set, we randomly selected 50 unique images that were not part of the training set to assess model performance. In the case of the CAVE dataset, 30 images were meticulously chosen for testing purposes, each boasting a spatial resolution of 512×512 pixels

and comprising 31 spectral bands, ensuring a comprehensive evaluation across diverse spectral characteristics and spatial attributes.

To evaluate the model’s generalization, testing datasets also encompass remote sensing datasets including the Washington DC dataset, real datasets: Urban [33].

3) *Comparison Methods and Evaluation Metrics*: Our experiments encompass a comparative analysis between HSDM and a spectrum of methodologies, including traditional model-based approaches including LRTDTV [34] and LLRGTV [7], as well as deep learning-based methods like GRNet [35], MACNET [24], T3SC [36], SST [37], SERT [27], and HSDT [38]. Notably, we specifically focus on contrasting our architecture against SST, SERT, and HSDT, which are all Transformer-based methods, aiming to underscore the denoising advantages inherent in our approach. To comprehensively evaluate the performance of these methodologies, we employ three distinct image quality evaluation metrics: Peak Signal-to-Noise Ratio (PSNR), Structural Similarity (SSIM) [39], and Spectral Angle Mapper (SAM) [40]. Through this meticulous comparison, we aim to elucidate the superior denoising capabilities of HSDM in various real-world scenarios.

4) *Noise Settings*: We conduct experiments by adding various levels of Gaussian noise and complex noise combinations to clean images. Each type of noise is applied with specific settings as outlined below:

- **Non-i.i.d. Gaussian Noise**: Zero-mean Gaussian noise, with intensities ranging randomly from 10 to 70, is added to each spectral band of the HSI.
- **Non-i.i.d. Gaussian + Stripe Noise**. In addition to the Gaussian noise, stripes are introduced randomly to one-third of the bands in the column. The proportion of stripes within each selected band varies from 5% to 15%.
- **Non-i.i.d. Gaussian + Deadline Noise**. Similar to Gaussian + Stripe Noise, but with deadline noise replacing stripe noise.
- **Non-i.i.d. Gaussian + Impulse Noise**. Gaussian noise is added to each band as in Non-i.i.d. Gaussian Noise, and impulse noise with intensities ranging from 10% to 70%



TABLE I  
QUANTITATIVE COMPARISON ON ICVL DATASETS WITH GAUSSIAN NOISE LEVELS. BEST IN **BOLD**, SECOND BEST UNDERLINED.

Methods	10			30			50			70		
	PSNR	SSIM	SAM	PSNR	SSIM	SAM	PSNR	SSIM	SAM	PSNR	SSIM	SAM
Noisy	28.13	0.8792	0.3267	18.59	0.5523	0.6622	14.15	0.3476	0.8554	11.23	0.2301	0.9851
LRTDTV [34]	40.05	0.9642	0.1523	37.58	0.9414	0.1137	35.68	0.9180	0.1756	34.22	0.8951	0.2534
LLRGTV [7]	42.30	0.9864	0.1256	36.36	0.9494	0.1394	33.06	0.9015	0.2756	30.76	0.8495	0.3283
GRNet [41]	36.12	0.9764	0.0933	36.17	0.9796	0.0888	29.64	0.9220	0.2174	29.64	0.9220	0.2174
MAC-Net [24]	41.30	0.9945	0.0540	38.45	0.9903	0.0818	35.36	0.9846	0.1000	32.70	0.9758	0.1205
T3SC [36]	43.70	0.9961	0.0449	40.62	0.9934	0.0514	37.87	0.9878	0.0675	35.17	0.9776	0.1042
QRNN3D [10]	44.75	0.9972	0.0370	42.50	0.9959	0.0359	40.45	0.9936	0.0409	38.33	0.9902	0.0500
SST [37]	44.75	0.9972	0.0370	42.50	0.9959	0.0359	40.45	0.9936	0.0409	38.33	0.9902	0.0500
SERT [27]	46.03	0.9981	0.0342	42.92	0.9964	<b>0.0334</b>	40.64	0.9940	<b>0.0390</b>	38.69	0.9910	0.0477
HSDT [38]	<b>47.04</b>	<b>0.9985</b>	<b>0.0260</b>	<b>42.95</b>	<u>0.9964</u>	<u>0.0341</u>	40.76	<u>0.9942</u>	<u>0.0400</u>	<u>39.24</u>	<u>0.9918</u>	<u>0.0455</u>
HSDM	<u>46.31</u>	<u>0.9982</u>	<u>0.0289</u>	<u>42.74</u>	<b>0.9964</b>	0.0362	<b>40.77</b>	<b>0.9943</b>	0.0408	<b>39.39</b>	<b>0.9922</b>	<b>0.0447</b>

is introduced randomly to one-third of the bands.

- Mixture Noise. Combines all the noise settings from the previous setting, randomly applied to each band.

5) *Implementation Details*: We introduce the random addition of complex noise from the first four noises during network training to improve the network’s adaptability and resilience. HSDM utilizes the Adam optimizer to minimize the mean squared error, following a training strategy similar to that outlined in [30], with minor modifications in the learning rate schedule. Specifically, the learning rate undergoes three stages: initially set to  $3e-4$ , it is then reduced by a factor of 5 after every 20 epochs. Training is performed with a batch size of 8 on an RTX3090 for 100 epochs.

B. Efficiency analysis

In this subsection, we analyze the performance of different methods regarding model parameter size and time consumption cost on the CAVE dataset with noise case 5. All test experiments are conducted on a 3090 GPU, and the results are presented in Table III.

HSDM showcases outstanding performance through its implementation of the Transformer-based architecture, striking a remarkable balance between computational efficiency and parameter optimization. Unlike other deep learning methodologies, it boasts accelerated computation times while maintaining a commendable equilibrium between resource utilization and performance metrics.

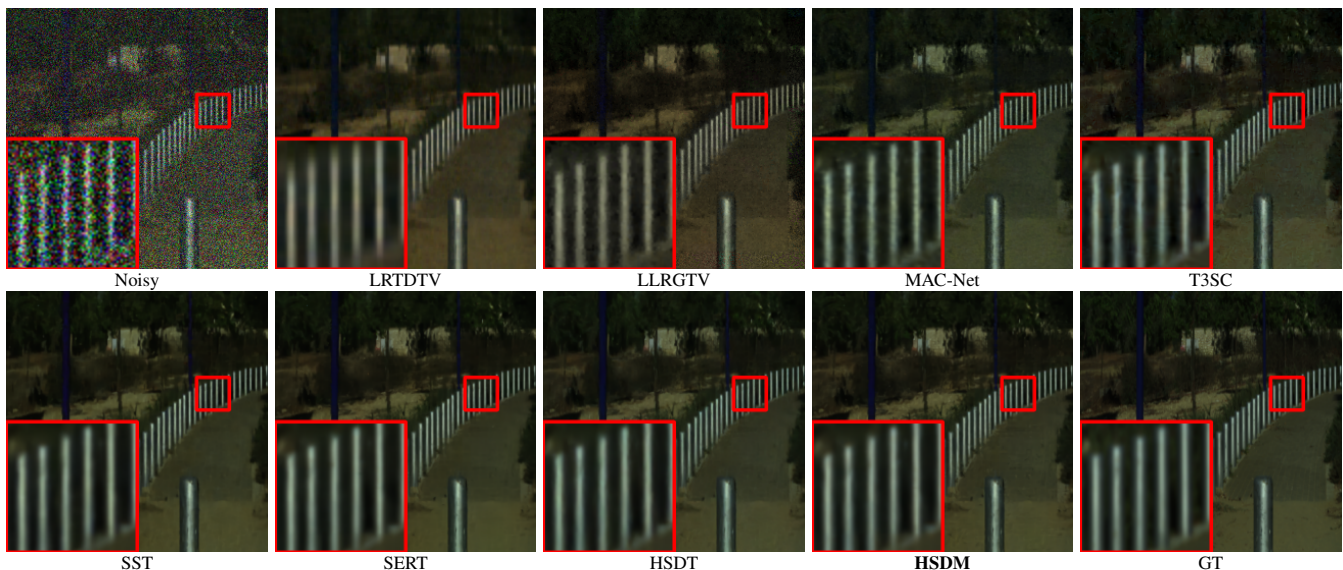


Fig. 4. Visual comparison of denoising on the ICVL dataset under Gaussian noise levels. The HSI bands 29, 19, and 9 combine to create the visual image.

TABLE II  
 QUANTITATIVE COMPARISON ON VARIOUS DATASETS UNDER MIXTURE NOISE. BEST IN **BOLD**, SECOND BEST UNDERLINED.

Methods	Noniid			Stripe			Deadline			Impulse			Mixture		
	PSNR	SSIM	SAM	PSNR	SSIM	SAM	PSNR	SSIM	SAM	PSNR	SSIM	SAM	PSNR	SSIM	SAM
Noisy	18.04	0.5056	0.8116	17.42	0.4826	0.8258	17.60	0.4852	0.8334	14.99	0.3811	0.8795	13.97	0.3392	0.8987
LRTDTV [34]	37.62	0.9434	0.1113	36.74	0.9375	0.1207	35.67	0.9289	0.1327	36.73	0.9373	0.1307	34.46	0.9184	0.1431
LLRGTV [7]	35.29	0.9381	0.1087	34.99	0.9352	0.1130	33.67	0.9186	0.1234	33.12	0.8958	0.1247	31.39	0.8756	0.1406
NGMeet [8]	34.85	0.9427	0.1412	34.25	0.9309	0.1508	33.48	0.9282	0.1437	30.00	0.8407	0.1448	28.98	0.8333	0.1431
QRNN3D [10]	42.06	0.9948	0.0501	41.63	0.9943	0.0525	41.74	0.9947	0.0514	40.35	0.9915	0.0741	39.22	0.9904	0.0809
GRNet [41]	34.55	0.9757	0.0937	34.18	0.9743	0.0989	33.13	0.9715	0.0969	32.46	0.9575	0.1461	31.67	0.9557	0.1431
MAC-Net [42]	39.84	0.9922	0.0764	39.01	0.9909	0.0730	36.95	0.9873	0.0966	34.56	0.9555	0.1899	30.75	0.9332	0.2673
T3SC [43]	41.83	0.9944	0.0525	41.24	0.9937	0.0583	39.54	0.9923	0.0856	37.94	0.9836	0.1151	35.68	0.9790	0.1389
SST [12]	<u>43.59</u>	0.9966	<u>0.0354</u>	<u>43.11</u>	0.9963	<u>0.0366</u>	42.98	0.9960	<u>0.0372</u>	42.18	0.9952	0.0424	39.58	0.9928	0.0480
SERT [13]	<b>43.65</b>	<b>0.9969</b>	<b>0.0343</b>	<b>43.18</b>	<b>0.9967</b>	<b>0.0359</b>	<b>43.24</b>	<b>0.9967</b>	<b>0.0362</b>	42.25	0.9953	<u>0.0420</u>	40.44	0.9940	<u>0.0470</u>
HSDT [38]	43.40	0.9965	0.0372	42.96	0.9962	0.0400	<u>43.02</u>	0.9963	0.0391	<u>42.27</u>	<u>0.9956</u>	0.0442	<u>40.76</u>	<u>0.9940</u>	0.0505
HSDM (Ours)	43.44	<u>0.9967</u>	0.0371	43.03	<u>0.9964</u>	0.0388	42.99	<u>0.9964</u>	0.0391	<b>42.43</b>	<b>0.9958</b>	<b>0.0418</b>	<b>41.30</b>	<b>0.9950</b>	<b>0.0459</b>

C. Experimental Results

To ensure the effectiveness of the comparative methods, for model-based approaches, we select corresponding test settings, and for deep learning-based methods, we compare them with their publicly available pre-trained models. All models are trained on the ICVL dataset. For datasets with a larger number of spectral bands, some comparative methods are only applicable to data with 31 spectral bands. We employ a sliding window strategy for denoising, and the average of the results within all windows is used as the final result.

1) *Complex Noise on Synthetic Datasets:* In this section, we investigate the denoising performance of various methods under fixed Gaussian noise with different standard deviations ( $\sigma$ ) ranging from 10 to 70, applied to the original HSI dataset. Our method is meticulously evaluated against baseline approaches on the ICVL dataset, with the comparative

outcomes meticulously detailed in Table I. Furthermore, to provide a comprehensive visual assessment, Figure 4 displays the denoising results obtained using different methods, among which HSDM exhibits superior performance overall, particularly evident at the noise level of  $\sigma = 70$ .

Upon scrutiny of the visual results, it is discerned that while LRTDTV, LLRGTV, and MAC-Net exhibit discernible pseudo-artifacts under the imposed Gaussian noise, our proposed HSDM method demonstrates superior efficacy in effectively eliminating Gaussian noise artifacts. Notably, HSDM adeptly preserves intricate details within the HSI dataset, thus ensuring superior fidelity and accuracy compared to alternative denoising techniques.

2) *Complex Noise on Synthetic Datasets:* To evaluate the denoising effectiveness in diverse noise environments, we undertake thorough comparative analyses of our approach across multiple datasets, encompassing synthetic datasets ICVL and

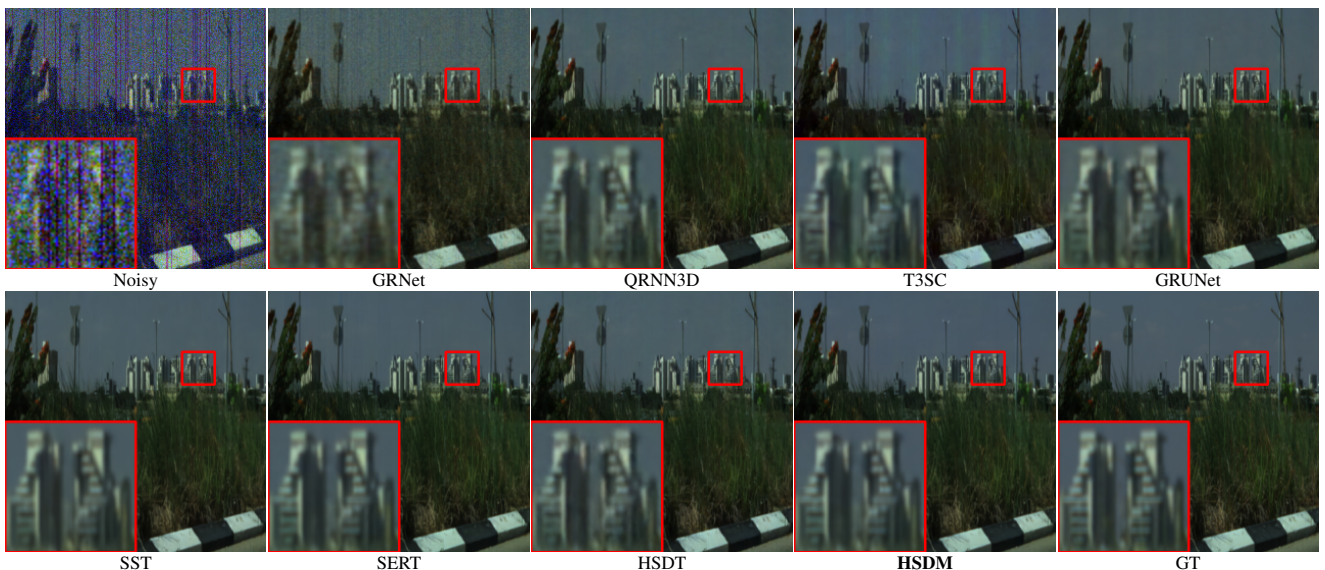


Fig. 5. Visual comparison of denoising on the ICVL dataset under mixture noise. The HSI bands 29, 19, and 9 combine to create the visual image.



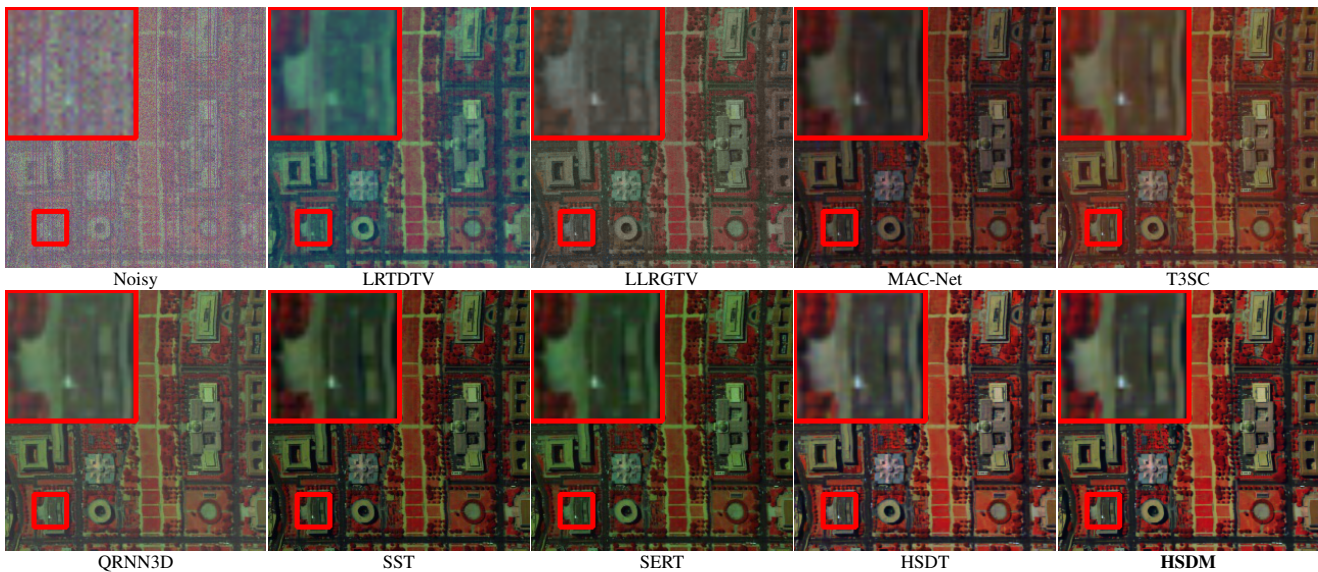


Fig. 6. Visual comparison of denoising on the WDC dataset under mixture noise. Bands 76, 43, and 10 combine to create the visual image.

TABLE III  
MODEL COMPLEXITY COMPARISONS ON THE CAVE DATASET WITH DIMENSIONS OF 512x512x31.

Methods	Params(M)	Times(s)	PSNR	SSIM	SAM
LLRT [44]	-	807.21	24.59	0.5795	0.8171
LRTDTV [34]	-	97.65	33.82	0.9085	0.2938
LLRGTV [7]	-	171.72	27.12	0.7221	0.6567
NGMMeet [8]	-	86.03	23.20	0.6229	0.7874
QRNN3D [10]	0.86	1.01	36.55	0.9825	0.4244
GRNet [41]	41.44	<b>0.63</b>	28.44	0.8899	0.6329
MACNet [42]	<b>0.43</b>	3.09	28.53	0.8920	0.6234
T3SC [43]	0.83	1.06	33.61	0.9728	0.4137
GRUNet [45]	14.28	1.94	35.98	0.9764	0.4049
SST [12]	4.10	3.36	34.89	0.9616	0.4095
SERT [13]	1.91	1.29	35.86	0.9737	0.3403
HSDM(Ours)	<u>0.68</u>	<u>0.77</u>	<b>35.99</b>	<b>0.9867</b>	<b>0.3221</b>

CAVE and remote sensing datasets like Urban and WDC. Table II delineates the performance metrics, including quantization and noise reduction, specifically for the ICVL dataset under varied noise scenarios. In experiments involving mixture noise variations within the ICVL dataset, HSDM consistently outshines HSDT, showcasing an improvement in PSNR of 0.54 dB.

Furthermore, visual comparison results under mixed noise settings on the ICVL dataset are presented in Figure 5. It is noteworthy to observe a spectral shift phenomenon in denoising outcomes obtained with GRNet, wherein certain pixels transition from yellow to blue hues. Similarly, T3SC exhibits noticeable color distortion issues. In stark contrast, our proposed MambaHSID model maintains superior spectral consistency and visual fidelity, closely aligning with the GroundTruth across both spectral and spatial domains.

3) *Noise on Real World:* To validate the model’s robustness under real-world noise conditions, we conducted hyperspectral

image denoising experiments on representative datasets Urban. Figures 7 illustrate the visual denoising performance across Urban datasets.

Moreover, we extended our denoising experiments to include the CAVE dataset, and the quantitative outcomes are detailed in Table IV. HSDM showcased remarkable superiority in real noise removal, as evidenced by its higher PSNR and SSIM values compared to other methods. While LRTDTV and LLRGTV demonstrated a certain degree of alignment with the SAM metric changes on real datasets due to their priori global low-rank assumptions, their performance was relatively poorer on additional datasets. In contrast, HSDM consistently exhibited superior performance across a wider range of datasets, underscoring its versatility and adaptability to various HSI denoising scenarios.

#### D. Ablation experiment

1) *Effectiveness of scanning mechanism:* To better explore the impact of scanning mechanisms combined with SSM on HSI denoising, we conducted experiments using both popular Sweep scanning and adjacent scanning methods on different datasets. We performed both unidirectional and bidirectional experiments for each scanning method, and the results are summarized in Table IV. The findings provide evidence supporting the effectiveness of our bidirectional adjacent scanning approach.

Despite the varying number of individual scan iterations required by different scanning mechanisms in the comparative experiments, we ensure uniformity in the total number of scans by selecting a specific scanning strategy at each layer, thereby maintaining a consistent model size across all variations.

Results demonstrate that our bidirectional adjacent scanning approach outperforms other scanning methods, indicating its effectiveness in capturing complex spatial-spectral relationships within the hyperspectral data. This finding underscores the importance of considering bidirectional scanning mecha-



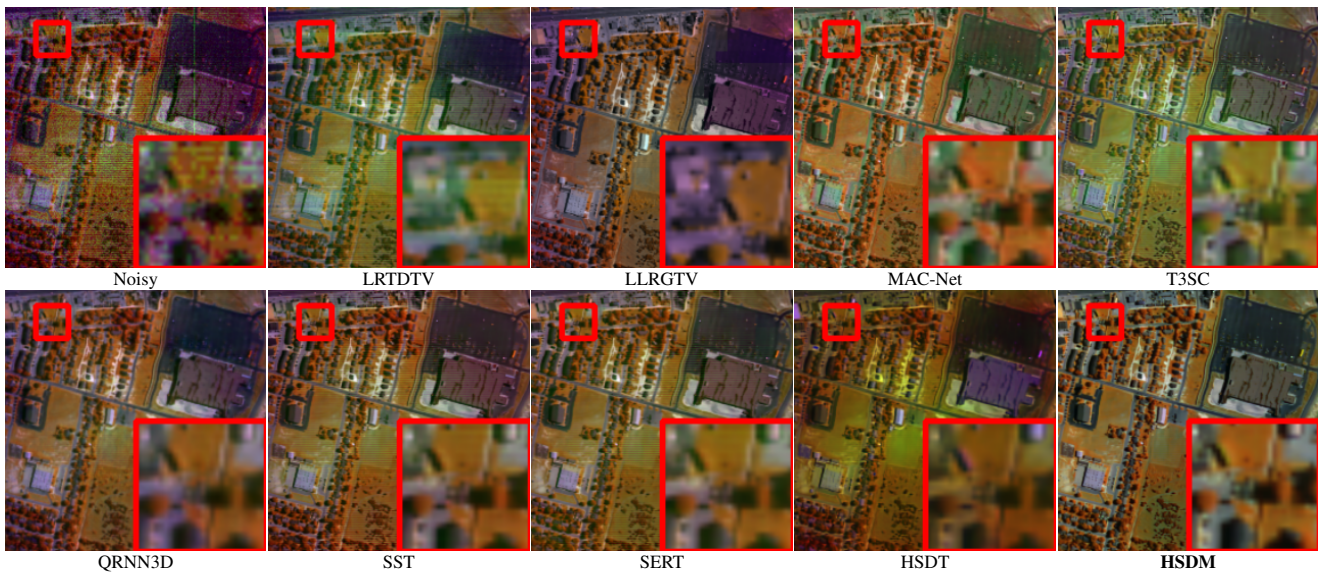


Fig. 7. Visual comparison of denoising on the Urban dataset. The HSI bands 102,138 and 202 combine to create the visual pseudocolor image.

TABLE IV

ABLATION STUDY ON THE SCANNING MECHANISM ON THREE DATASETS UNDER MIXTURE NOISE.

Baseline	Params(M)	ICVL		CAVE		WDC	
		PSNR	SSIM	PSNR	SSIM	PSNR	SSIM
Sweep	0.68	38.73	0.9911	35.19	0.9783	36.88	0.9872
Bid-Sweep	0.68	39.61	0.9936	35.42	0.9782	37.24	0.9881
Cross	0.68	39.17	0.9884	36.38	0.9832	37.19	0.9871
Bid-Cross	0.68	41.30	0.9950	35.99	0.9867	37.57	0.9890

TABLE V

ABLATION STUDY OF DIFFERENT ATTENTION WINDOW MECHANISMS ON ICVL DATASET UNDER MIXTURE NOISE.

Method	PSNR(dB)	SSIM	SAM
Baseline	41.30	0.9950	0.0459
Baseline + w/o Conv1D	41.09	0.9945	0.0293
Baseline + w/o Channel Attention	39.87	0.9934	0.0351

nisms when implementing state space models for HSI denoising.

2) *Effectiveness of modifications*: To enhance the effectiveness of the original Mamba module for HSI denoising, we have introduced several enhancements. Firstly, we have incorporated Conv1D operations to optimize the processing of linear sequences, thereby enhancing the model’s capacity to capture both spatial and spectral dependencies. Furthermore, we have integrated channel attention mechanisms specifically designed for HSI, aimed at further enriching the capabilities of the Mamba framework. The results of these enhancements are summarized in Table V.

3) *Comparison of the hidden dims*: The impact of varying numbers of hidden channels on the model’s feature-capturing ability is significant. We analyzed different numbers of hidden channels, presented in Table VI. This decision strikes a better

TABLE VI

ABLATION STUDY OF DIFFERENT SPECTRAL ENHANCEMENT STRATEGIES ON ICVL DATASET UNDER MIXTURE NOISE.

hidden dim	Params(M)	PSNR(dB)	SSIM	SAM
24	0.24	38.85	0.9901	0.0418
36	0.44	39.71	0.9936	0.0350
48	0.68	41.30	0.9950	0.0459
64	1.08	41.50	0.9937	0.0374
96	2.17	41.76	0.9946	0.0360

balance between the model’s efficiency and performance considerations. By increasing the number of hidden channels to 48, the model gains enhanced capacity to capture and represent complex features within the data. This decision contributes to improved model performance without excessively increasing computational complexity, thus optimizing the trade-off between efficiency and effectiveness.

### E. Parameter analysis

HSDM consistently maintains its GPU memory consumption and FPS rate, even with gradually increasing blocks. In contrast, the primary baseline Bidirectional HSDM experiences a decrease in FPS due to increased parameters. Notably, HSDM Mamba, with blocks of 4, performs faster without altering parameters. Study on block sizes ranging from 2, 4, 6, to 8 reveals a deterioration, highlighting the importance of block sizes for optimal performance. Too few blocks may reduce effective feature extraction, while too many may lead to feature redundancy. Targeted selection of the block size balances computational efficiency and model effectiveness, ensuring effective feature capture while maintaining efficient processing speeds.

## V. CONCLUSION

In this paper, we present HSIDMamba(HSDM), an innovative HSI denoising approach grounded in the selective state space model framework. HSDM is engineered to tackle the unique obstacles associated with processing long sequences inherent in HSI. By seamlessly integrating convolution and attention mechanisms, HSDM excels at capturing intricate spatial-spectral dependencies with remarkable computational efficiency, thanks to its linear complexity. Moreover, it introduces a novel bidirectional continuous scanning mechanism meticulously tailored to the nuances of HSI, thereby amplifying its ability to perceive and process spatial-spectral information effectively. Through extensive experimental validations conducted across diverse datasets, HSDM surpasses existing methodologies, highlighting its effectiveness and efficiency in tackling the challenges of HSI denoising.

## REFERENCES

- [1] N. Aburaed, M. Q. Alkhatib, S. Marshall, J. Zabalza, and H. Al Ahmad, "A review of spatial enhancement of hyperspectral remote sensing imaging techniques," *IEEE Journal of Selected Topics in Applied Earth Observations and Remote Sensing*, vol. 16, pp. 2275–2300, 2023.
- [2] X. He, C. Tang, X. Liu, W. Zhang, K. Sun, and J. Xu, "Object detection in hyperspectral image via unified spectral-spatial feature aggregation," *IEEE Transactions on Geoscience and Remote Sensing*, 2023.
- [3] J. Jang, S. Oh, Y. Kim, D. Seo, Y. Choi, and H. J. Yang, "Sodai: Multi-modal maritime object detection dataset with rgb and hyperspectral image sensors," *Advances in Neural Information Processing Systems*, vol. 36, 2024.
- [4] J. Yang, B. Du, D. Wang, and L. Zhang, "Iter: Image-to-pixel representation for weakly supervised hsi classification," *IEEE Transactions on Image Processing*, 2023.
- [5] Y. Ding, Z. Zhang, X. Zhao, D. Hong, W. Cai, N. Yang, and B. Wang, "Multi-scale receptive fields: Graph attention neural network for hyperspectral image classification," *Expert Systems with Applications*, vol. 223, p. 119858, 2023.
- [6] L. Sun and B. Jeon, "Hyperspectral mixed denoising via subspace low rank learning and bm4d filtering," in *IGARSS 2018-2018 IEEE International Geoscience and Remote Sensing Symposium*. IEEE, 2018, pp. 8034–8037.
- [7] W. He, H. Zhang, H. Shen, and L. Zhang, "Hyperspectral image denoising using local low-rank matrix recovery and global spatial-spectral total variation," *IEEE Journal of Selected Topics in Applied Earth Observations and Remote Sensing*, vol. 11, no. 3, pp. 713–729, 2018.
- [8] W. He, Q. Yao, C. Li, N. Yokoya, and Q. Zhao, "Non-local meets global: An integrated paradigm for hyperspectral denoising," 2019, pp. 6868–6877.
- [9] J. Guan, R. Lai, H. Li, Y. Yang, and L. Gu, "Dnrcnn: Deep recurrent convolutional neural network for hsi destriping," *IEEE Transactions on Neural Networks and Learning Systems*, 2022.
- [10] K. Wei, Y. Fu, and H. Huang, "3-d quasi-recurrent neural network for hyperspectral image denoising," vol. 32, no. 1, pp. 363–375, 2020.
- [11] S. Khan, M. Naseer, M. Hayat, S. W. Zamir, F. S. Khan, and M. Shah, "Transformers in vision: A survey," *ACM computing surveys (CSUR)*, vol. 54, no. 10s, pp. 1–41, 2022.
- [12] M. Li, Y. Fu, and Y. Zhang, "Spatial-spectral transformer for hyperspectral image denoising," vol. 37, no. 1, 2023, pp. 1368–1376.
- [13] M. Li, J. Liu, Y. Fu, Y. Zhang, and D. Dou, "Spectral enhanced rectangle transformer for hyperspectral image denoising," 2023, pp. 5805–5814.
- [14] A. Gu, K. Goel, and C. Ré, "Efficiently modeling long sequences with structured state spaces," *arXiv preprint arXiv:2111.00396*, 2021.
- [15] J. Smith, A. Warrington, and S. Linderman, "Simplified state space layers for sequence modeling," Aug 2022.
- [16] D. Y. Fu, T. Dao, K. K. Saab, A. W. Thomas, A. Rudra, and C. Ré, "Hungry hungry hippos: Towards language modeling with state space models," *arXiv preprint arXiv:2212.14052*, 2022.
- [17] H. Mehta, A. Gupta, A. Cutkosky, and B. Neyshabur, "Long range language modeling via gated state spaces," Jun 2022.
- [18] A. Gu and T. Dao, "Mamba: Linear-time sequence modeling with selective state spaces," Dec 2023.
- [19] K. Li, X. Li, Y. Wang, Y. He, Y. Wang, L. Wang, and Y. Qiao, "Videomamba: State space model for efficient video understanding," *arXiv preprint arXiv:2403.06977*, 2024.
- [20] H. Guo, J. Li, T. Dai, Z. Ouyang, X. Ren, and S.-T. Xia, "Mambair: A simple baseline for image restoration with state-space model," *arXiv preprint arXiv:2402.15648*, 2024.
- [21] V. T. Hu, S. A. Baumann, M. Gui, O. Grebenkova, P. Ma, J. Fischer, and B. Ommer, "Zigma: Zigzag mamba diffusion model," *arXiv preprint arXiv:2403.13802*, 2024.
- [22] Q. Zhang, Q. Yuan, J. Li, X. Liu, H. Shen, and L. Zhang, "Hybrid noise removal in hyperspectral imagery with a spatial-spectral gradient network," *IEEE Transactions on Geoscience and Remote Sensing*, vol. 57, no. 10, pp. 7317–7329, 2019.
- [23] Q. Yuan, Q. Zhang, J. Li, H. Shen, and L. Zhang, "Hyperspectral image denoising employing a spatial-spectral deep residual convolutional neural network," *IEEE Transactions on Geoscience and Remote Sensing*, vol. 57, no. 2, pp. 1205–1218, 2018.
- [24] F. Xiong, J. Zhou, Q. Zhao, J. Lu, and Y. Qian, "Mac-net: Model-aided nonlocal neural network for hyperspectral image denoising," *IEEE Transactions on Geoscience and Remote Sensing*, vol. 60, pp. 1–14, 2021.
- [25] S. Mei, C. Song, M. Ma, and F. Xu, "Hyperspectral image classification using group-aware hierarchical transformer," *IEEE Transactions on Geoscience and Remote Sensing*, vol. 60, pp. 1–14, 2022.
- [26] Y. Cai, J. Lin, X. Hu, H. Wang, X. Yuan, Y. Zhang, R. Timofte, and L. Van Gool, "Mask-guided spectral-wise transformer for efficient hyperspectral image reconstruction," in *Proceedings of the IEEE/CVF Conference on Computer Vision and Pattern Recognition*, 2022, pp. 17 502–17 511.
- [27] M. Li, J. Liu, Y. Fu, Y. Zhang, and D. Dou, "Spectral enhanced rectangle transformer for hyperspectral image denoising," in *Proceedings of the IEEE/CVF Conference on Computer Vision and Pattern Recognition*, 2023, pp. 5805–5814.
- [28] J. X. Yang, J. Zhou, J. Wang, H. Tian, and A. W. C. Liew, "Hsimamba: Hyperspectral imaging efficient feature learning with bidirectional state space for classification," *arXiv preprint arXiv:2404.00272*, 2024.
- [29] Y. Yue and Z. Li, "Medmamba: Vision mamba for medical image classification," *arXiv preprint arXiv:2403.03849*, 2024.
- [30] K. Wei, Y. Fu, and H. Huang, "3-d quasi-recurrent neural network for hyperspectral image denoising," *IEEE transactions on neural networks and learning systems*, vol. 32, no. 1, pp. 363–375, 2020.
- [31] B. Arad and O. Ben-Shahar, "Sparse recovery of hyperspectral signal from natural rgb images," in *Computer Vision—ECCV 2016: 14th European Conference, Amsterdam, The Netherlands, October 11–14, 2016, Proceedings, Part VII 14*. Springer, 2016, pp. 19–34.
- [32] J.-I. Park, M.-H. Lee, M. D. Grossberg, and S. K. Nayar, "Multispectral imaging using multiplexed illumination," 2007, pp. 1–8.
- [33] V. Mnih and G. E. Hinton, "Learning to detect roads in high-resolution aerial images." Springer, 2010, pp. 210–223.
- [34] Y. Wang, J. Peng, Q. Zhao, Y. Leung, X.-L. Zhao, and D. Meng, "Hyperspectral image restoration via total variation regularized low-rank tensor decomposition," *IEEE Journal of Selected Topics in Applied Earth Observations and Remote Sensing*, vol. 11, no. 4, pp. 1227–1243, 2017.
- [35] Z. Kuang, Y. Gao, G. Li, P. Luo, Y. Chen, L. Lin, and W. Zhang, "Fashion retrieval via graph reasoning networks on a similarity pyramid," in *Proceedings of the IEEE/CVF international conference on computer vision*, 2019, pp. 3066–3075.
- [36] T. Bodrito, A. Zouaoui, J. Chanussot, and J. Mairal, "A trainable spectral-spatial sparse coding model for hyperspectral image restoration," *Advances in Neural Information Processing Systems*, vol. 34, pp. 5430–5442, 2021.
- [37] M. Li, Y. Fu, and Y. Zhang, "Spatial-spectral transformer for hyperspectral image denoising," in *Proceedings of the AAAI Conference on Artificial Intelligence*, vol. 37, no. 1, 2023, pp. 1368–1376.
- [38] Z. Lai, C. Yan, and Y. Fu, "Hybrid spectral denoising transformer with guided attention," 2023, pp. 13 065–13 075.
- [39] Z. Wang, A. C. Bovik, H. R. Sheikh, and E. P. Simoncelli, "Image quality assessment: from error visibility to structural similarity," *IEEE transactions on image processing*, vol. 13, no. 4, pp. 600–612, 2004.
- [40] R. H. Yucas, J. W. Boardman, and A. F. Goetz, "Determination of semi-arid landscape endmembers and seasonal trends using convex geometry spectral unmixing techniques," in *JPL, Summaries of the 4th Annual JPL Airborne Geoscience Workshop. Volume 1: AVIRIS Workshop*, 1993.

- [41] X. Cao, X. Fu, C. Xu, and D. Meng, “Deep spatial-spectral global reasoning network for hyperspectral image denoising,” vol. 60, pp. 1–14, 2021.
- [42] F. Xiong, J. Zhou, Q. Zhao, J. Lu, and Y. Qian, “Mac-net: Model-aided nonlocal neural network for hyperspectral image denoising,” vol. 60, pp. 1–14, 2021.
- [43] T. Bodrito, A. Zouaoui, J. Chanussot, and J. Mairal, “A trainable spectral-spatial sparse coding model for hyperspectral image restoration,” vol. 34, pp. 5430–5442, 2021.
- [44] Y. Chang, L. Yan, and S. Zhong, “Hyper-laplacian regularized unidirectional low-rank tensor recovery for multispectral image denoising,” 2017, pp. 4260–4268.
- [45] Z. Lai, K. Wei, and Y. Fu, “Deep plug-and-play prior for hyperspectral image restoration,” *Neurocomputing*, vol. 481, pp. 281–293, 2022.